Acta Astronautica 109 (2015) 112–123

Contents lists available at ScienceDirect

Acta Astronautica

journal homepage: www.elsevier.com/locate/actaastro

Optimal propellantless rendez-vous using differential drag

L. Dell'Elce *, G. Kerschen

Université de Liège, Aerospace & Mechanical Engineering Department, S3L, Chemin des Chevreuils, 1, 4000 Liège, Belgium

ARTICLE INFO

Article history:
Received 22 July 2014
Received in revised form
8 November 2014
Accepted 12 January 2015
Available online 19 January 2015

Keywords:
Differential drag
Optimal control
6-Degree-of-freedom
QB50

ABSTRACT

Optimization of fuel consumption is a key driver in the design of spacecraft maneuvers. For this reason, growing interest in propellant-free maneuvers is observed in the literature. Because it allows us to turn the often-undesired drag perturbation into a control force for relative motion, differential drag is among the most promising propellantless techniques for low-Earth orbiting satellites. An optimal control approach to the problem of orbital rendez-vous using differential drag is proposed in this paper. Thanks to the scheduling of a reference maneuver by means of a direct transcription, the method is flexible in terms of cost function and can easily account for constraints of various nature. Considerations on the practical realization of differential-drag-based maneuvers are also provided. The developments are illustrated by means of high-fidelity simulations including coupled 6-degree-of-freedom simulations and an advanced aerodynamic model.

1. Introduction

Optimization is a key factor in mission design, especially when dealing with formation flying, where severe size and weight constraints may strongly limit the performance of the propulsive system. Nowadays, propellantless techniques for formation flying, e.g., solar sail [1], geomagnetic [2], and Coulomb formation flying [3], are envisaged as possible solutions to either reduce or even remove the need for onboard propellant. This paper focuses on a propellantless technique based on the differential drag concept. By controlling the surface exposed to the residual atmosphere, it is possible to change the magnitude of the atmospheric drag and therefore to create a differential force, between one spacecraft (chaser) and either another spacecraft or a desired target point. This force can be exploited to control the relative position between the chaser and the target in the orbital plane, which enhances the maneuverability of small satellites in low-Earth orbits (LEO). Specifically, nanosatellites are becoming popular because of their modest cost and development time. Differential drag provides them with an effective means to perform long range relative maneuvers with an arguably large flexibility.

The exploitation of differential drag for LEO spacecraft was first introduced by Leonard [4], who developed a strategy for controlling the cross section aimed at achieving a rendez-vous within the linear dynamics equations of Hill–Clohessy–Wiltshire. The idea of decomposing the relative motion into a mean and a harmonic component was also proposed in order to gain deep insight into the physical behavior of the problem. However, the methodology relied upon several restrictive assumptions, including circular orbits, a point mass Earth, and a uniform atmosphere. Motivated by the desire to consider more representative scenarios, Bevilacqua et al. included the secular perturbations of the Earth's oblateness in Leonard's method [5]. They also proposed a hybrid approach combining differential drag and continuous low-thrust [6] aimed at enhancing out-of-plane controllability. Finally, a novel approach for bang–bang control based on an adaptive Lyapunov control strategy was developed to account for nonlinear orbital dynamics [7]. Kumar and Ng implemented the solution in a high-precision

* Corresponding author. Tel.: +3243669449.
E-mail address: lamberto.dellelce@ulg.ac.be (L. Dell'Elce).

http://dx.doi.org/10.1016/j.actaastro.2015.01.011
0094-5765/

propagator [8] and they highlighted the importance of accurate mean states estimation in order to prevent the solution from drastic deterioration. Lambert et al. [9] overcame this issue by exploiting a conversion from osculating to mean orbital elements of both the target and the chaser. Targeting long-term cluster keeping and collision avoidance using differential drag, Ben-Yaacov et al. [10] proposed a nonlinear control approach based on mean and osculating differential elements, respectively.

This large body of literature emphasizes that differential drag is regarded as a promising technique for LEO satellites, since it allows us to turn the often-undesired drag perturbation into a control force for relative motion. This results into the reduction, or even the removal, of propellant needs for some missions and into a consistent weight and volume saving. Nonetheless, relevant uncertainties in drag modeling make its practical realization a challenge, especially if no other propulsive means is available to accommodate them. The ORBCOMM constellation is the first application of the differential drag technique in space, though it is only limited to station-keeping [11]. The forthcoming missions QARMAN, JC2sat, and SAMSON highlight the overall interest in the technique [12–14].

The present study has a twofold objective:

- First, a novel formulation of the rendez-vous maneuver using differential drag is proposed. This is an improved version of the optimal control approach which we developed in [15]. The method consists of three main blocks, namely the drag estimator, the maneuver planner, and the on-line compensator. The drag estimation is carried out by means of a simple density model which, nonetheless, is able to detect the main features of the upper atmosphere. The planner is then in charge of the scheduling of an optimal reference path. A Radau pseudospectral transcription is exploited for the numerical resolution. This results in an extreme flexibility for the choice of the cost function, and it facilitates the inclusion of constraints of arbitrary nature. Though Ben-Yaacov et al. and Kumar et al. [10,16] proposed continuous control approaches, most of the literature on differential drag considers the bang–bang control of the cross section. When the relative ballistic coefficient is imposed through attitude control, the assumption of bang–bang control is restrictive, especially for small satellites with limited power available. The proposed formulation results in time-continuous control of the cross section. Finally, online compensation relying on a model predictive control (MPC) algorithm is implemented to account for uncertainties and unmodeled dynamics.
- Second, some practical challenges that are intimately related to the exploitation of the differential drag in a realistic scenario are addressed. For this purpose, high-fidelity 6-degree-of-freedom (DoF) propagation including advanced drag modeling and detailed space environment are exploited to validate the algorithm. As an example, we note that the entire literature on differential drag assumes that drag is proportional to the cross-section of the spacecraft and that it is the only component of the aerodynamic force. Realistic drag modeling is clearly missing in the literature on differential drag and it is therefore considered in this paper. In addition, the present paper assumes that the two satellites have different geometries, which result in different ballistic properties.

The paper is organized as follows. The rendez-vous problem and the notations are defined in Section 2. Section 3 describes the different building blocks of the proposed optimal control strategy. The simulation environment is detailed in Section 4. Numerical simulations based on the QARMAN mission are detailed in Section 5. Finally, Section 6 summarizes the main results of this study and discusses the future directions of our work.

2. Modeling assumptions and reference frames

This study focuses on the rendez-vous problem between two satellites, namely the target and the chaser, using differential drag as the only control force. It is assumed that the orbits of the satellites are near-circular and quasi-coplanar. Though the former assumption could be eventually removed, it is not the case for the latter, which comes from the extremely modest authority of the differential drag in the out-of-plane direction. Specifically, Ben-Yaacov et al. showed that the controllability is two orders of magnitude smaller in this direction even for highly inclined orbits [17]. For this reason, *only the in-plane position and velocity of the relative dynamics are controlled herein*.

The reference frames and the coordinates exploited in the paper are defined as follows:

- *Mean local vertical local horizontal* (*LVLH*) *frame*: The origin is in the target. The $\hat{\boldsymbol{x}}$ and $\hat{\boldsymbol{z}}$ axes point toward the mean position vector and the mean orbital momentum of the target,respectively. The $\hat{\boldsymbol{y}}$-axis completes the right-hand frame. In what follows,in-plane mean relative curvilinear coordinates, $(\tilde{x}, \tilde{y}, \tilde{v}_x, \tilde{v}_y)$,and their decomposition into mean and oscillatory components of the trajectory, $(\tilde{x}_m, \tilde{y}_m, \tilde{x}_o, \tilde{y}_o)$,are exploited instead of the Cartesian mean relative position and velocity, (x, y, v_x, v_y). The graphical interpretation of the curvilinear coordinates is illustrated in Fig. 1(b). We point out that a twofold use of the word 'mean' is done to indicate both the averaging of the orbital elements and the mean component of the relative trajectory. The decomposition of the curvilinear states into mean and oscillatory component is such that $\tilde{x} = \tilde{x}_m + \tilde{x}_o$ and $\tilde{y} = \tilde{y}_m + \tilde{y}_o$. In order to ease the flow of the discussion, the operations involved in the definition of these variables are postponed to Appendix A.
- *Chaser's body frame*. The origin is in the center of mass of the chaser. The $\hat{\boldsymbol{x}}_b, \hat{\boldsymbol{y}}_b$, and $\hat{\boldsymbol{z}}_b$ axes form a right-hand frame and they are aligned with the principal axes of the chaser.

These frames are illustrated in Fig. 1(a).

Differential drag is imposed by changing the ballistic coefficient of the chaser. This can be achieved either by means of the reorientation of solar panels or through attitude control. The second option is considered herein,

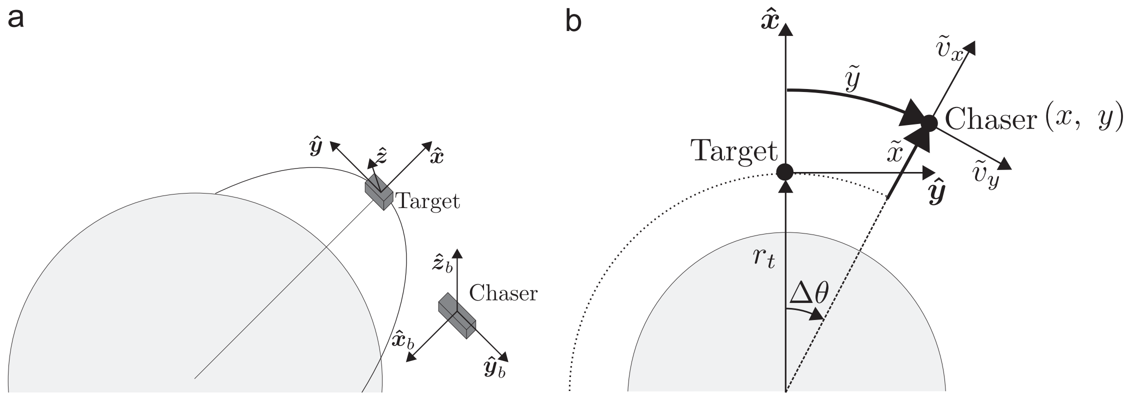

Fig. 1. Frames and coordinates. (a) Reference frames. (b) Cartesian and curvilinear coordinates.

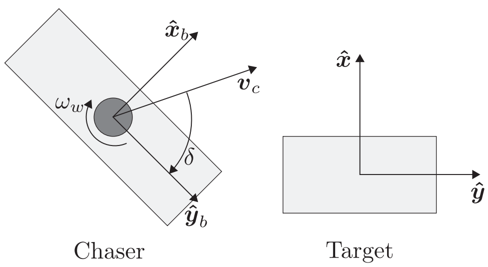

Fig. 2. Attitude dynamics of the chaser. The target is supposed to fly with the long axis aligned to the orbital velocity direction.

this is resulting into the coupling between rotational and translational degrees of freedom. Depending on the specific actuators considered, attitude constraints of various nature are introduced into the problem. In this paper, the combination of three reaction wheels and 3-axis magnetotorquers is exploited. The resulting constraints are the saturation of the wheel's momentum and their maximum available torque, and the maximum dipole of the magnetotorquers.

The target is assumed to be passive, i.e., its ballistic coefficient cannot be controlled. *The proposed methodology is only applicable if the attitude of the target is predictable.* This includes not only fully-stabilized configurations, but also spinning and tumbling satellites. Scheduled maneuvers can be included as well. On the contrary, the method fails if the target performs, for example, attitude and orbital maneuvers or solar panel reconfigurations which were not expected before the beginning of the rendez-vous maneuver. Without loss of generality, it is supposed that the target is 3-axis stabilized in its minimum-drag configuration. The same methodology applies for spinning and tumbling target, while minor modifications should be included to account for prescribed maneuvers of the target.

Because the satellites considered in the case study in Section 5 are CubeSats without deployable panels, they are modeled with a parallelepiped shape and the principal axes are assumed to be aligned with the edges of the parallelepiped. This is very appropriate when considering satellites with body-mounted solar arrays. The contribution to the aerodynamic force and torque of possible appendices, e.g., antennas, is neglected. This assumption facilitates the computation of the aerodynamic force in the high-fidelity simulations and the notations in the paper. However, it does not jeopardize the generality of the proposed formulation, which is *independent from the specific geometry*, provided that minimum and maximum drag configuration of the chaser are identified.

Considering the scheme in Fig. 2, the reference attitude of the two satellites is such that:

- the target's long axis is toward its orbital velocity direction, $\boldsymbol{v}_t$;
- the $\hat{\boldsymbol{z}}_b$ axis is toward $\hat{\boldsymbol{z}}$. The magnitude of the differential drag is changed by pitching the chaser about $\hat{\boldsymbol{z}}_b$. The pitching angle is given by

$$\delta = \cos^{-1}\left(\frac{\boldsymbol{v}_c}{\|\boldsymbol{v}_c\|}\cdot\hat{\boldsymbol{y}}_b\right)\operatorname{sign}(\boldsymbol{v}_c\cdot\hat{\boldsymbol{x}}_b), \tag{1}$$

where $\boldsymbol{v}_c$ is the osculating orbital velocity of the chaser and $\hat{\boldsymbol{y}}_b$ is toward the long axis of the chaser.

3. Optimal control approach

The proposed optimal control strategy consists of three modules: (i) the drag estimator evaluates the ballistic coefficient of the two satellites, (ii) the maneuver planner schedules an optimal reference trajectory, (iii) the on-line compensator corrects the deviations from the reference path due to unmodeled dynamics and uncertainties. The high-level control strategy is illustrated in Fig. 3.

The drag estimator and the maneuver planner are activated only a few times during the complete maneuver, e.g., they could be executed either when the divergence between the real and the planned path is beyond a given threshold or after a fixed time-step of one-to-few days.[1] In this work, we execute these two modules once at the beginning.

Targeting a computationally-efficient formulation of the problem, the dynamical system exploited by the controller, named the *control plant*, cannot account for all the complex dynamics characterizing the high-fidelity

[1] In the experience of the authors, the maximum update rate of the reference path should not go beyond 5 days.

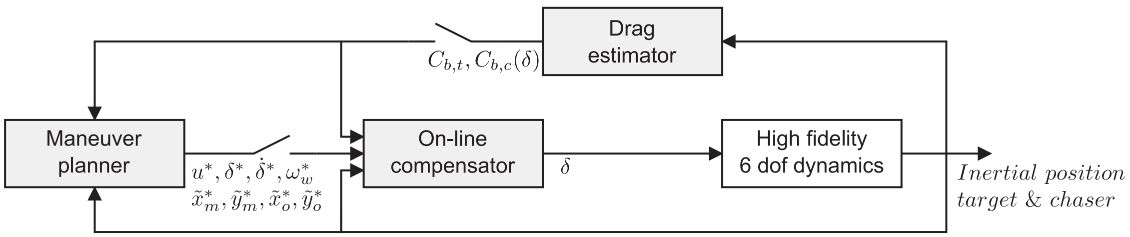

Fig. 3. High-level optimal control strategy. The asterisk denotes the reference trajectory and control.

simulation environment. The definition of the control plant requires the introduction of a certain number of underlying assumptions discussed in the following.

First, drag is assumed to be the only component of the aerodynamic force, the ballistic coefficient is constant and fitted with a polynomial function of the exposed surface to the incoming wind. Section 3.1 provides with more details on the estimation of the ballistic properties of the satellites.

Second, considering the scheme illustrated in Fig. 2 and the notations of Section 2, the control plant assumes that the attitude of the target is three-axis stabilized, while the attitude of the chaser is stabilized in the $\hat{\boldsymbol{x}}_b$ and $\hat{\boldsymbol{y}}_b$ directions. The rotation about the $\hat{\boldsymbol{z}}_b$ direction of the chaser is controlled via a reaction wheel with inertia I_w, maximum torque T_w, angular velocity with respect to the spacecraft ω_w, and operating range $[\omega_{w,l}, \omega_{w,u}]$. Unlike the other methods proposed in the literature, the controlled variable, u, is not the differential drag, but the torque provided to the reaction wheel. Magnetotorquers are exploited to desaturate the wheel in permanence by introducing a torque in the $\hat{\boldsymbol{z}}_b$ direction that is proportional to $-\omega_w$. So, the pitch angle δ, its time derivative, and ω_w are the only attitude dynamics variables introduced in the control plant.

Finally, as anticipated in Section 2, only the in-plane movement is considered. The translational dynamics equations of the control plant are expressed in terms of mean decomposed curvilinear relative states, which are smoother than the Cartesian or the curvilinear coordinates. This facilitates the convergence of the optimization problem discussed in Section 3.1.

Thus, the dynamic variables considered by the controller are $\tilde{x}_m$, $\tilde{y}_m$, $\tilde{x}_o$, $\tilde{y}_o$, δ, $\dot{\delta}$, and ω_w.

3.1. Drag estimator

This module is in charge of the estimation of the ballistic properties of the two satellites. For this purpose, it requires that their accurate position is monitored for an observation time t_{obs}. The attitude of the satellites is imposed throughout this period.

If a single pose is sufficient for the determination of the ballistic coefficient of the target, this is not the case for the chaser. The reason is that the ballistic coefficient is not proportional to the cross section. A number of $n_{pose} \geq 2$ poses with different pitch angles δ_i, $i = 1, \dots, n_{pose}$ must be observed. Each pose is monitored for a time equal to t_{obs}/n_{pose}. A trade-off between the accuracy and the duration of the estimation is mandatory. Because the real environment is largely more complex than the control plant, e.g., the controller assumes that the ballistic coefficient does only depend on the pitch angle, we suggest that the number of poses must be kept as small as possible.

The ballistic coefficient is estimated by minimizing the drift between observed and simulated inertial positions. Simulated data are generated on-board through a low-precision propagation including J_2 gravitational effect and drag perturbation only. The aerodynamic force of the simulated data is given by

$$\boldsymbol{F}_d = -\tfrac{1}{2}\rho C_b \|\boldsymbol{v}_{TAS}\| \boldsymbol{v}_{TAS} \tag{2}$$

where $\boldsymbol{v}_{TAS} = \boldsymbol{v} - \boldsymbol{\Omega}_e \times \boldsymbol{r}$, C_b, ρ, $\boldsymbol{r}$, $\boldsymbol{v}$, and $\boldsymbol{\Omega}_e$ are the airspeed, the ballistic coefficient, the atmospheric density, the inertial position and velocity, and the Earth's angular velocity, respectively. A basic analytical model is exploited to estimate the density:

$$\rho(r, \theta, i; A, B, C, D) = A(1 + B\cos(\theta - C)) \exp\left(\frac{r - r_e\sqrt{1 - e_e^2 \sin^2 i \sin^2 \theta}}{D}\right) \tag{3}$$

where θ, i, (A, B, C, D), r_e, and e_e, are the mean argument of latitude and orbital inclination, the calibration coefficients of the model, and the Earth's equatorial radius and eccentricity, respectively. Though relatively simple, this model is able to outline the more relevant characteristics of the upper atmosphere, namely the exponential vertical structure, the day–night bulge, and the Earth's oblateness. Neglecting these contributions results into inconsistent predictions of the short-term evolution of the density, e.g., the day–night bulge is responsible for variations of approximatively a factor of 5 at 500 km according to [27], which lead to the generation of an unreliable reference path (see Section 3.2).

The coefficients of the model are orbit-dependent and they are tuned using a more advanced model, i.e., Jacchia 71 in this work, by minimizing the root mean square error between the density provided by Eq. (3) and the advanced model during one orbit.

The estimation is performed by solving:

$$C_{b,t} = \arg\left[\min_{C_b}\left(\int_0^{t_{obs}} (\boldsymbol{r}_{obs,t} - \boldsymbol{r}_{sim,t}(C_b))^2 \,\mathrm{d}t\right)\right]$$

$$C_{b,c}(\delta_i) = \arg\left[\min_{C_b}\left(\int_{(t_{obs}/n_{pose})(i-1)}^{(t_{obs}/n_{pose})i} (\boldsymbol{r}_{obs,c} - \boldsymbol{r}_{sim,c}(C_b))^2 \,\mathrm{d}t\right)\right],$$
$$i = 1, \dots, n_{pose} \tag{4}$$

Here, $\boldsymbol{r}_{obs}$ and $\boldsymbol{r}_{sim}$ are the observed and simulated inertial position, respectively. The subscripts t and c indicate the target and the chaser, respectively. The process of the

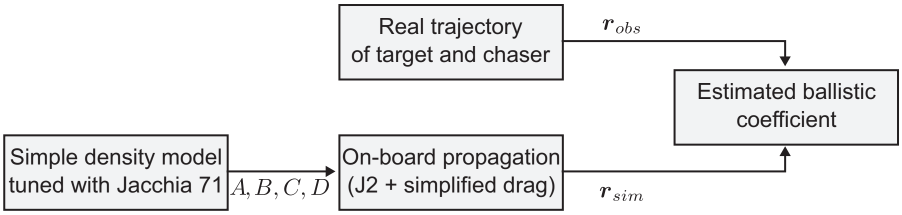

Fig. 4. Schematic representation of the estimation of the ballistic coefficient.

computation of the ballistic coefficient is illustrated in Fig. 4.

The necessary condition for the exploitation of the differential drag is that the estimated ballistic coefficient of the target must be such that $\min(C_{b,c}(\delta_i)) < C_{b,t} < \max(C_{b,c}(\delta_i))$. In this case, the target is said to be feasible. Finally, the ballistic coefficient of the chaser is fitted with a polynomial of order $n_{pose}-1$ in function of the exposed cross section

$$S = S_x|\sin\ \delta| + S_y|\cos\ \delta| \tag{5}$$

where S_x and S_y are the surface of the faces of the chaser with normal $\hat{\boldsymbol{x}}_b$ and $\hat{\boldsymbol{y}}_b$, respectively.

The outputs of the drag estimator are the fitted ballistic coefficient of the chaser, $C_{b,c}(\delta)$, and the constant ballistic coefficient of the target, $C_{b,t}$.

3.2. Maneuver planner

The maneuver planner schedules an optimal reference trajectory for the rendez-vous maneuver. The trade-off between computational cost and accuracy is the key driver of the synthesis of the planner.

The optimal control problem is solved with a *hp*-adaptive Radau pseudospectral transcription [19] using the software GPOPS. Direct transcriptions are arguably the most flexible way to deal with optimal control problems because constraints of various nature can be naturally included in the formulation. The core idea of direct techniques is the discretization of the time history of the state and control variables. Dynamics equations are then enforced as equality constraints in a nonlinear programming (NLP) problem. The design variables of the NLP are the state and control variables in the grid points. Four main blocks constitute every pseudospectral method: function generator (i.e., dynamics equations), discretization, optimization, convergence analysis. Specifically, GPOPS tackles the discretization by means of an implicit Gaussian quadrature based on the *Legendre–Gauss–Radau* collocation points. This approach lends to an *hp*-adaptive strategy for the convergence analysis and mesh refinement. The optimization is carried out by means of the sparse solver SNOPT.

The maneuver planning problem is posed in the Bolza form

$$u^*(t) = \arg\left[\min_{u(t)}\left(\int_0^{t_f} \mathcal{L}(\tilde{x}_m, \tilde{y}_m, \tilde{x}_o, \tilde{y}_o, \delta, \dot{\delta}, \omega_w, u, t)\, \mathrm{d}t\right)\right]$$

subject to (6)

$$\omega_w \in [\omega_{w,l}, \omega_{w,u}], \quad |u| \le T_w,$$

$$|M_{mag}(\omega_w, t)| \le M_{mag,max}(t) \quad \forall\ t \in [0, t_f] \tag{7}$$

$$\tilde{x}_m(0) = \tilde{x}_{m,0}, \quad \tilde{x}_o(0) = \tilde{x}_{o,0}, \quad \delta(0) = \delta_0, \quad \dot{\delta}(0) = 0$$

$$\tilde{y}_m(0) = \tilde{y}_{m,0}, \quad \tilde{y}_o(0) = \tilde{y}_{o,0}, \quad \omega_w(0) = \omega_{w,0} \tag{8}$$

$$\tilde{x}_m(t_f) = \tilde{y}_m(t_f) = \tilde{x}_o(t_f) = \tilde{y}_o(t_f) = 0 \tag{9}$$

$$\begin{cases} \dot{\tilde{x}}_m = \dfrac{2c}{(2-c^2)\omega}\Delta F_d(\delta, \tilde{x}_m + \tilde{x}_o, \tilde{y}_m + \tilde{y}_o, t) \\ \dot{\tilde{y}}_m = \dfrac{(2-5c^2)\omega}{2c}\tilde{x}_m \\ \dot{\tilde{x}}_o = \dfrac{(2-c^2)\omega}{2c}\ \tilde{y}_o - \dfrac{2c}{(2-c^2)\omega}\Delta F_d(\delta, \tilde{x}_m + \tilde{x}_o, \tilde{y}_m + \tilde{y}_o, t) \quad \forall t \in [0, t_f] \\ \dot{\tilde{y}}_o = -2\omega c \tilde{x}_o \\ \ddot{\delta} = I_{zz}^{-1}((\boldsymbol{r}_{cg} \times \boldsymbol{F}_{d,c}) \cdot \hat{\boldsymbol{z}}_b - M_{mag}(\omega_w, t) - u) \\ \dot{\omega}_w = (I_{zz}^{-1} + I_w^{-1})u - I_{sat}^{-1}\ ((\boldsymbol{r}_{cg} \times \boldsymbol{F}_{d,c}) \cdot \hat{\boldsymbol{z}}_b - M_{mag}(\omega_w, t)) \end{cases} \tag{10}$$

where ω, c, I_{zz}, ΔF_d, u, M_{mag}, and $\boldsymbol{r}_{cg}$ are the orbital angular velocity, the Schweighart–Sedwick coefficient (defined in Appendix A) the rotational inertia of the chaser without the reaction wheel about the $\hat{\boldsymbol{z}}_b$ direction, the estimated differential drag, the torque provided by the reaction wheel, the de-saturating torque of the magnetic rods, and the position of the center of mass of the chaser in the body frame, respectively.

The initial guess for the NLP is provided by the analytical solution of Bevilacqua et al. [7]. As in the case of our control plant, this solution relies on the linearized Schweighart–Sedwick equations of relative motion [18], but it provides a bang–bang control for the differential drag, whose magnitude is assumed to be constant. The maneuvering time, t_f, is determined by the initial guess and it is not part of the design variables of the problem.

The performance index, defined in Eq. (6), is aimed at minimizing a desired convex functional, $\mathcal{L}$, to be chosen according to the needs of the mission. Few examples include the dissipated to collected power ratio, i.e., consumption of the attitude control system over the incoming solar power, the mean squared differential drag (as discussed in Section 5.2), the optimization of a geometrical feature of the trajectory (as shown later in Eq. (14)).

Physical constraints include the maximum available torque, the operating range of the wheel, and the saturation of the magnetic coils. They are naturally introduced through the path constraints of Eq. (7).

Eqs. (8) and (9) express the initial and rendez-vous conditions, respectively.

The differential equations (10) govern the relative movement and attitude dynamics. Since the direct transcription enforces dynamics equations as equality constraints in a NLP optimization problem, the proper choice of the differential equations is the core of the trade-off between accuracy and computational efficiency of the planner:

- the planner is required to be consistent with the real dynamics. Consistency implies that *all* the dominant effects are modeled. This includes short-period and altitude-dependent variations of the drag. When propagating the open-loop control, we observed that neglecting short-period variations reflects in inconsistent predictions of the oscillatory movement, while neglecting altitude dependency results in larger in-track errors at the end of the maneuver.
- targeting computational efficiency, we want that *only* the dominant effects are modeled in the planner. This excludes all the orbital perturbations but the drag and secular J_2 effects. The same simplified drag modeling of the drag estimation module is used, i.e., Eqs. (2) and (3). We note that the aerodynamic force must be projected in the orbital velocity direction to yield the differential drag. Assuming circular orbits, it holds

$$\Delta F_d = \left(\mathcal{R}_z\left(-\frac{\tilde{y}}{r_t+\tilde{x}}\right)\boldsymbol{F}_{d,c}(\tilde{x},\tilde{y},t)-\boldsymbol{F}_{d,t}(t)\right)\cdot\hat{\boldsymbol{y}} \qquad (11)$$

  where $\mathcal{R}_z$ is the rotation matrix about the $\hat{\boldsymbol{z}}$ direction. Further efficiency is achieved by expressing relative dynamics in terms of decomposed curvilinear variables, which are ‘smoother’ and more decoupled than relative states. Finally, in our previous method [20], the right-hand term of the differential equation directly accounted for nonlinear dynamics, as illustrated by the solid path in Fig. 5. Considering linearized dynamics (dotted path) largely enhances computational efficiency with limited loss of accuracy.

We stress that the *only* input of the planner are the initial conditions and the outputs of the drag estimator.

The outputs of the planner are the reference control and states in function of time, namely u^*, $\tilde{x}_m^*$, $\tilde{y}_m^*$, $\tilde{x}_o^*$, $\tilde{y}_o^*$, δ^*, $\dot{\delta}^*$, ω_w^*.

3.3. On-line compensator

On-line compensation is mandatory to account for unmodeled dynamics and uncertainties. The former issue arises from the assumptions introduced in the definition of the control plant. In addition, the density model of the drag estimator is another source of unmodeled dynamics, because different atmospheric models generate different outputs given the same inputs. The latter issue reflects the practical difficulties in the prediction of stochastic processes like the solar and geomagnetic activity proxies and thermospheric winds [21].

No matter the origin, the effect of all these perturbations is the deviation of the observed trajectory from the scheduled path. A model predictive control algorithm is developed to cope with such deviations.

At each evaluation, the on-line compensator solves a problem analogous to the maneuver planner. The only differences are the boundary conditions, the fixed horizon, and the performance index.

Initial conditions are provided by the current states at the beginning of the evaluation at time t. MPC is based upon the receding horizon principle, i.e., the final time is fixed to $t+t_h$, where t_h is the horizon. The computed corrected control is then applied to the plant for a time $t_c \le t_h$.

The performance index is aimed at minimizing the divergence from the reference path

$$\int_t^{t+t_h}[W_{x,m}(\tilde{x}_m-\tilde{x}_m^*)^2+W_{x,o}(\tilde{x}_o-\tilde{x}_o^*)^2+W_{y,m}(\tilde{y}_m-\tilde{y}_m^*)^2 + W_{y,o}(\tilde{y}_o-\tilde{y}_o^*)^2+W_\delta(\delta-\delta^*)^2+W_{\dot{\delta}}\dot{\delta}^2]\,d\tau \qquad (12)$$

where $W_{(\cdot)}$ are user-defined weights. A direct contribution of the controlled variable is not included, because its variation is dominated by the variations of δ. $W_{\dot{\delta}}$ is aimed at minimizing spurious oscillations of the pitch angle. The proper selection of the weights is not trivial, and stability issues may arise. Large W_δ means high confidence in the reference path, but a less efficient tracking of the reference trajectory itself. We tested different setups with initial in-track distances ranging up to 300 km. Setting coefficients such that the three contributions have the same order of magnitude resulted in a stable controller within this range. However, our future research will investigate a robust and automatic procedure for tuning the coefficients. Ideally, a large W_δ is more suitable for the first phase of the maneuver.

4. Simulation environment

The numerical simulations of the rendez-vous maneuver performed in this study are carried out in a highly-detailed environment. Both attitude and orbital dynamics of the target and the chaser are propagated in their complete nonlinear coupled dynamics.

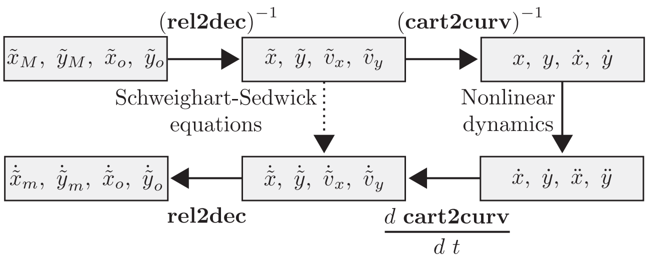

Fig. 5. Schematic representation of the computation of the right hand term of the translational differential equations of the controller. Computational efficiency is achieved using the linearized equations of motion. The nomenclature of the operators is detailed in Appendix A.

Table 1
Differences. between the simulation environment and the plant of the controller.

	Simulation environment	Control plant
Orbital dynamics	Full nonlinear osculating relative dynamics.	Linearized equations for mean curvilinear relative states.
Attitude dynamics	3 DoF Euler equations.	Single DoF dynamics about the pitch axis.
Atmospheric model	NRLMSISE-00 with short-term stochastic variations. Geodetic altitude from the reference ellipsoid.	Exponential vertical structure and sinusoidal periodic variations (day-night). Geocentric altitude from the reference ellipsoid.
Aerodynamic force	Sentman's model with more recent updates.	Drag force only. Cubic polynomial fitting of the estimated ballistic coefficients with the different poses.
Gravitational model	Harmonics up to order and degree 10.	J_2 secular effect.
Other perturbations	Luni-solar third-body perturbations, solar radiation pressure. Nutation, precession and polar wandering.	None.
External torques	Gravity gradient and aerodynamic torque computed with Sentman's model and more recent updates.	Simplified aerodynamic torque consisting of the cross product between the drag and the aerodynamic-to-gravity center distance vector.
Attitude control	Three-axis magnetic coils and three reaction wheels. Quaternion feedback control algorithm. Magnetic coils desaturate wheels in permanence.	Single reaction wheel about the pitch angle. Magnetic coils desaturate the wheel in permanence. The control torque is determined by the planner and on-line compensator.

The orbital perturbations include aerodynamic force, a detailed gravitational field with harmonics up to order and degree 10, solar radiation pressure and third-body perturbations of sun and moon. The external torques are due to aerodynamics and gravity gradient, and the models proposed by Wertz [22] for the reaction wheels and magnetic rods are exploited.

In this study, the modeling of the aerodynamic perturbation assumes thermal flow, variable accommodation of the energy, and non-zero re-emission velocity. Under these hypotheses, the three extensively-used simplifications involved in drag modeling fall into defect. Specifically, it is not true that the drag is the only component of the aerodynamic force, that the drag coefficient is constant, and that the drag is proportional to the surface exposed to the incoming flow. In Section 5, we show that abandoning these simplifying assumptions has impact on the maneuver's accuracy.

A large body of literature on the determination of physical aerodynamic coefficients is available, see, e.g., [23,24]. For complex satellite geometries, direct simulation Monte Carlo (DSMC) is arguably the only way of computing these coefficients. However, this technique is extremely computationally intensive. For simple convex geometries, semi-empirical analytic methods relying on the decomposition into elementary panels provide an accurate and computationally-effective alternative. The semi-analytic method considered in this work is based upon the research of Sentman [25] and Cook [26] and upon more recent contributions. The method is efficiently summarized in Ref. [27].

This method was used in our orbital propagator to compute the aerodynamic coefficients of the satellites at every time step. An analogous model is used for the aerodynamic torque.

The atmospheric model exploited in the propagator is NRLMSISE-00 [28]. Short-term random variations are included by adding a second-order stationary stochastic process to the total mass density. The power spectral density of the process is the one proposed by Zijlstra [29] rescaled for the altitude of the maneuver. The atmosphere is assumed to co-rotate with the Earth, but thermospheric winds are neglected.

We note that the calibration of the simple model defined in Eq. (3) was not performed with the same model exploited for the high-fidelity simulations, i.e., Jacchia 71 and NRLMSISE-00, respectively. This is motivated by the scope of the paper to consider a realistic scenario. In this way, the controller does not know the exact structure of the atmosphere.

Table 1 summarizes the main features of the simulation environment and compares them to the counterpart of the control plant discussed in Section 3

For the sake of clarity, in the remainder of the paper we will refer to high-precision propagation with the adjectives ‘observed’ or ‘real’. This will avoid confusion with data generated by the control plant, which we will refer to as ‘simulated’.

5. Case study

The proposed case study consists of the rendez-vous between two satellites of the QB50 constellation [30]. QB50 will be a constellation of 40 double and 10 triple CubeSats [31]. The launch is planned for 2016. The constellation will be deployed on a highly-inclined near-circular LEO, and the satellites will be separated by several tens or hundreds kilometers.

The QB50 requirements for the ‘standard 2U CubeSats’ [32] impose that the long axis of the CubeSat must be aligned with the orbital velocity. One of these standard CubeSats is considered to be the target. QARMAN, a 3U CubeSat of the constellation developed by the Von Karman Institute for Fluid dynamics and the University of Liège, will be the chaser. Both the target and the chaser are assumed to be equipped with 3-axis magnetotorquers and 3 reaction wheels with spin axes aligned with the geometric axes of the CubeSat. Quaternion feedback algorithm [33] is exploited to follow the required attitude of the two satellites.

Table 2 lists the input parameters of the numerical simulations.

The results of the three different modules of the controller are analyzed separately in the following.

Table 2
Simulation parameters.

Mean elements of the target	Semi-major axis	6728×10^3 m
	Eccentricity	0.001
	Inclination	98 deg
	RAAN	45 deg
	Argument of perigee	0 deg
	True anomaly	0 deg
	Julian date	2,455,287.5 days
Initial relative states	In-track position, i.e., $\tilde{y}$	50×10^3 m
	Radial position, i.e., $\tilde{x}$	100 m
	Out-of-plane position, i.e., z	20 m
	In-track velocity, i.e., $\tilde{v}_y$	$0\ \mathrm{m\ s^{-1}}$
	Radial velocity, i.e., $\tilde{v}_x$	$0\ \mathrm{m\ s^{-1}}$
	Out-of-plane velocity, i.e., v_z	$0\ \mathrm{m\ s^{-1}}$
Initial target's attitude (LVLH)	Pitch, roll, yaw	0 deg
Initial chaser's attitude (LVLH)	Pitch, roll, yaw	0 deg
Space weather	Daily solar flux	200 sfu
	81-day averaged flux	155 sfu
	Geomagnetic index K_p	4
Target properties	Mass	2 kg
	Dimensions	$0.1 \times 0.2 \times 0.1\ \mathrm{m}^3$
	Inertia	$I_y = 8 \times 10^{-3}\ \mathrm{kg\ m^2}$, $I_x = I_z = 3 \cdot 10^{-3}\ \mathrm{kg\ m^2}$
	Offset of the center of mass	$0.01\boldsymbol{y}_b$ m
Chaser properties	Mass	4 kg
	Dimensions	$0.1 \times 0.3 \times 0.1\ \mathrm{m}^3$
	Inertia	$I_y = 25 \cdot 10^{-3}\ \mathrm{kg\ m^2}$, $I_x = I_z = 5 \cdot 10^{-3}\ \mathrm{kg\ m^2}$
	Offset of the center of mass	$0.01\boldsymbol{y}_b$ m
Attitude actuators	Wheels' maximum torque	$0.03 \cdot 10^{-3}$ N m
	Wheels' operating range	$[-6000, 6000]$ rpm
	Wheels' inertia	$0.25 \cdot 10^{-6}\ \mathrm{kg\ m^2}$
	Magnetic rods' dipole	$0.2\ \mathrm{A\ m^2}$
On-line compensator's weights	$W_{x,m},\ W_{y,m},\ W_{x,o},\ W_{y,o}$	$1\ \mathrm{m^{-2}}$
	W_δ	$10^4\ \mathrm{rad^{-2}}$
	$W_{\dot{\delta}}$	$10^8\ \mathrm{s^2\ rad^{-2}}$

5.1. Drag estimator

In this work, we selected $n_{pose} = 4$ and we observed each pose during 2 orbits, so that $t_{obs} = 2t_{orb}n_{pose} = 8t_{orb}$, where t_{orb} is the mean orbital period of the target.

Fig. 6 compares the real drag force of the target with the one estimated with the identified $C_{b,t}$ and the simplified density model of the drag estimator (Eq. (3)). As anticipated, the controller does not know the exact structure of the atmosphere. This is emphasized by the relevant difference between the estimated and the real drag force in Fig. 6. Nonetheless, the good match between the simple and the largely more advanced Jacchia 71 model, validates our claim stating that the former is able to detect the main features of the structure of the upper atmosphere.

5.2. Maneuver planner

The first cost function considered consists of the mean-squared differential drag:

$$\frac{1}{t_f}\int_{t_{obs}}^{t_{obs}+t_f} \Delta F_d^2(\tilde{x}, \tilde{y}, t)\, \mathrm{d}t. \tag{13}$$

This objective is aimed at achieving a trajectory that can be robustly followed: minimizing the differential drag used by the planner results in the maximization of the remaining differential drag that can be exploited to compensate for deviations from the reference path. In other words, this objective function avoids bang–bang-like solutions. This latter, in fact, is such that differential drag is for most of the time at its extreme values, so that on-line compensation cannot provide two-sided maneuverability. We note that the lower bound of the integral is t_{obs}, because the planned maneuver starts right after the observation period necessary for the estimation of the ballistic properties.

Fig. 7 illustrates the scheduled trajectory generated by the planner. The reference pitch exhibits a gradual transition from a maximum to a minimum differential drag configuration. This is consistent with the above explanation on the purpose of the cost function. At the end of the scheduled path, exact rendez-vous conditions are met, as imposed by Eqs. (9).

The interest in the proposed approach is its flexibility, i.e., the trajectory can be optimized according to the needs of the mission. Assume, for example, that a smooth relative trajectory is envisaged. The objective function of the planner can then be selected as follows:

$$\frac{1}{t_f}\int_{t_{obs}}^{t_{obs}+t_f} \left(\tilde{x}_o^2 + \tilde{y}_o^2\right) \mathrm{d}t \tag{14}$$

Fig. 8 illustrates the obtained solution considering this cost function. The benefit of the optimization process is

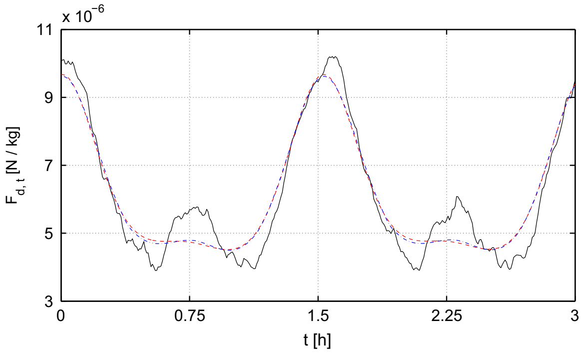

Fig. 6. Drag force of the target. The solid line is the real drag. The dashed line is the estimated drag with the simple atmospheric model. The dash-dot line is the estimated drag with the Jacchia 71 model.

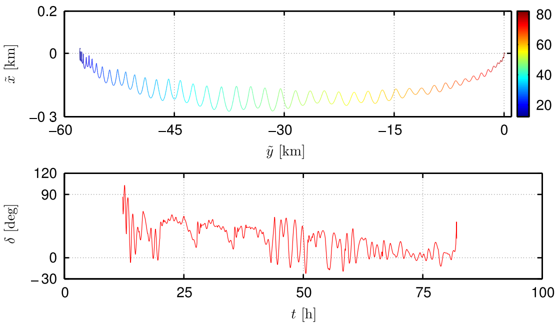

Fig. 7. Minimum-differential-drag off-line (i.e., scheduled) maneuver. In the upper figure, the color indicates the elapsed time since the beginning of the maneuver, including the drag estimation time. (For interpretation of the references to color in this figure caption, the reader is referred to the web version of this paper.)

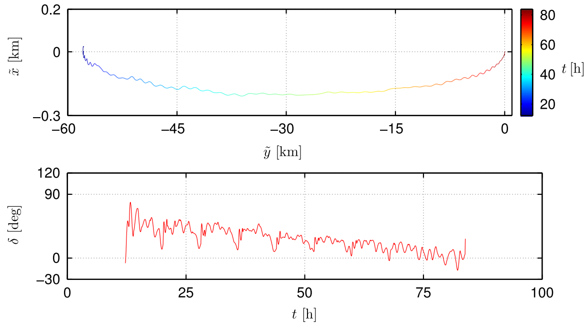

Fig. 8. 'Flattest trajectory' off-line maneuver (i.e., scheduled). In the upper figure, the color indicates the elapsed time since the beginning of the maneuver, including the drag estimation time. (For interpretation of the references to color in this figure caption, the reader is referred to the web version of this paper.)

evident. Achieving this trajectory with other approaches would be at best challenging.

We note that the initial position in Figs. 7 and 8 is different from the one provided in Table 2 because the reference path starts after the drag estimation phase. This gap emphasizes the importance of limiting the duration of such phase.

5.3. On-line compensator

The horizon and the control time of the on-line compensator are set to $t_h = 2t_c = 2t_{orb}$. This combination allows for an adequate averaging of short period variations that are the most critical to predict. The on-line controller is thus activated once per orbit, and it computes an open loop control with two-orbit horizon.

Fig. 9 illustrates the obtained trajectory in the high-fidelity simulations and the corrected pitch angle. The overshoot in the $\hat{\boldsymbol{y}}$ direction at the end of the scheduled maneuver, $t_f + t_{obs}$, is of the order of 250 m. In our opinion, the on-line compensator is able to track the reference path with an adequate accuracy, given the limitations and the uncertainties inherent to differential drag. For the sake of completeness, Fig. 10 depicts the on-line solution for the 'flat' trajectory.

The importance of the weights of the reference pitch angle and its derivative in the cost function of the on-line compensator is illustrated in Fig. 11. Here, the weights related to the tracking and the derivative of the pitch are removed from the objective function of the MPC algorithm, i.e., $W_\delta = W_{\dot{\delta}} = 0$. In this case, the quality of the tracking of the reference path is essentially unchanged, but the corrected pitch exhibits spurious oscillations. This time history of the pitch is more demanding for the attitude control system and results in larger power consumption.

The accuracy of the maneuver is affected by the assumptions used in the development of the control plant. This is shown in Fig. 12, where a zoom of the terminal phase of the maneuver is illustrated. The rendez-vous conditions are met with a precision of the order of 20 m, which is worse than the precision shown in previous works, e.g., [15]. This loss of accuracy needs to be considered when including collision avoidance constraints. The reason why it is not possible to improve the accuracy further is that the satellites have different geometries and masses. Recalling that the aerodynamic coefficients are computed on the actual geometry at every time step of the high-fidelity simulations and that drag is not proportional to the exposed surface, it follows that the real zero-differential drag configuration is unknown. In addition, the MPC algorithm is open-loop over the control horizon.

However, in our opinion, it is not the scope of differential-drag maneuvers to achieve the highest precision, especially given the limited out-of-plane controllability. In the numerical simulations, in fact, out-of-plane oscillations are of the same order of the accuracy of the terminal phase.

Finally, Fig. 13 shows that the method works also for very large initial relative distances. The tracking of the scheduled path is much less accurate but eventually the on-line compensator manages to achieve the success of the maneuver. For a better tracking, the scheduled path could be updated sporadically. Indeed, because the number of design variables grows up with the maneuvering time, the computational demand of the reference path is larger.

6. Conclusion

This paper proposed a three-step optimal control approach for differential-drag-based maneuvers. The method allows us to optimize the trajectory according to the needs of

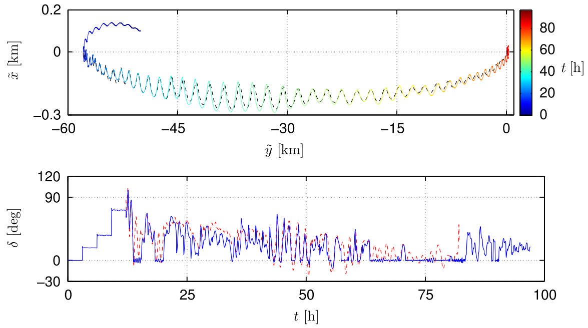

Fig. 9. Minimum-differential-drag on-line maneuver. In the upper figure, the black-dotted and the colored line are the planned and the on-line trajectories, respectively. The color indicates the elapsed time since the beginning of the maneuver, including the drag estimation time. In the bottom figure, the dashed and the solid lines are the scheduled and the on-line pitch angles, respectively. (For interpretation of the references to color in this figure caption, the reader is referred to the web version of this paper.)

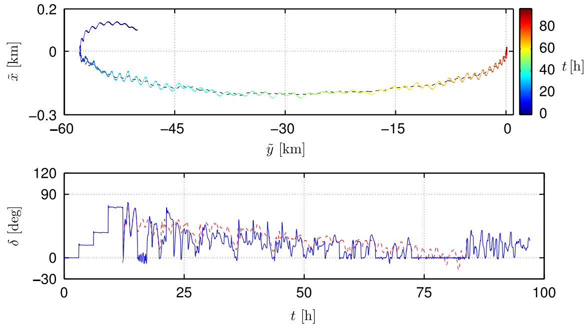

Fig. 10. 'Flattest trajectory' maneuver. In the upper figure, the black-dotted and the colored line are the planned and the on-line trajectories, respectively. The color indicates the elapsed time since the beginning of the maneuver, including the drag estimation time. In the bottom figure, the dashed and the solid lines are the scheduled and the on-line pitch angles, respectively. (For interpretation of the references to color in this figure caption, the reader is referred to the web version of this paper.)

the mission and to naturally include constraints of various nature within the problem, e.g., minimum distance or volume avoidance constraints.

The method was tested with high-precision simulations of a rendez-vous maneuver between satellites with different masses and geometries and advanced drag modeling.

Future work will further improve the scenario, i.e., by including thermospheric winds and realistic relative state estimation and acquisition, and identify and assess the importance of the uncertainty sources in the performance of the maneuver.

Acknowledgment

The author Lamberto Dell'Elce would like to acknowledge the Belgian National Fund for Scientific Research for its financial support (FRIA fellowship).

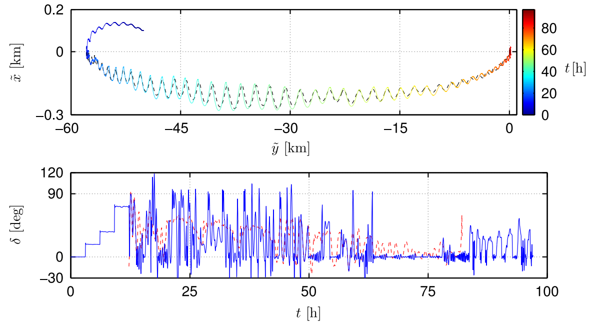

Fig. 11. Minimum-differential-drag on-line maneuver without tracking of the reference pitch angle. In the upper figure, the black-dotted and the colored line are the planned and the on-line trajectories, respectively. The color indicates the elapsed time since the beginning of the maneuver, including the drag estimation time. In the bottom figure, the dashed and the solid lines are the scheduled and the on-line pitch angles, respectively. (For interpretation of the references to color in this figure caption, the reader is referred to the web version of this paper.)

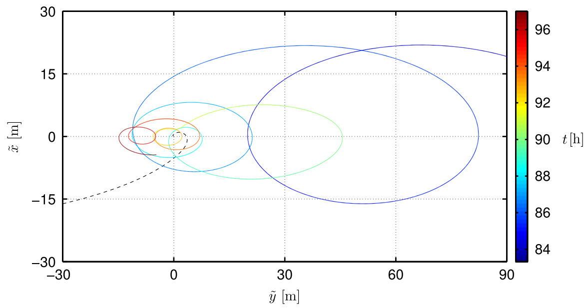

Fig. 12. Minimum-differential-drag on-line maneuver. Zoom of the terminal phase. The black-dotted and the colored line are the planned and the on-line trajectories, respectively. The color indicates the time since the beginning of the maneuver. (For interpretation of the references to color in this figure caption, the reader is referred to the web version of this paper.)

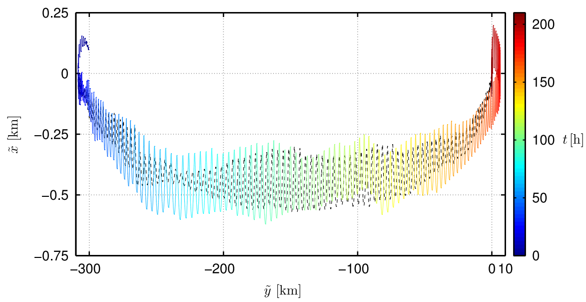

Fig. 13. Minimum-differential-drag long-range maneuver. The initial in-track relative position is 300 km. The black-dotted and the colored line are the planned and the on-line trajectories, respectively. The color indicates the elapsed time since the beginning of the maneuver, including the drag estimation time. (For interpretation of the references to color in this figure caption, the reader is referred to the web version of this paper.)

Appendix A. Variable transformations

This annex details the change of variables discussed in the paper.

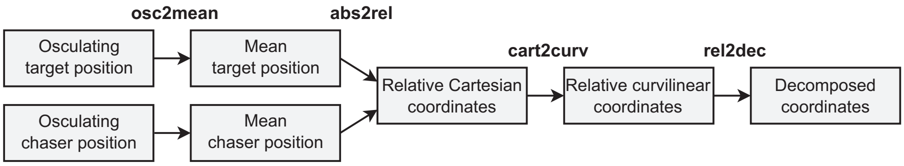

Fig. 14. Curvilinear relative state estimation from osculating orbital elements.

osc2mean: this transformation consists in: (1) mapping the osculating Earth centered inertial (ECI) coordinates into classical keplerian elements, (2) converting osculating to mean elements [34], (3) recovering mean cartesian position from the mean elements.

abs2rel: absolute coordinates are converted into relative states in the LVLH frame. In this paper, we only focus on the in-plane components, which we refer to as x and y.

cart2curv: curvilinear coordinates are mandatory for middle and long range maneuvers. Mapping relative to curvilinear coordinates is achieved through the transformation

$$\tilde{x} = \sqrt{(r_t+x)^2+y^2} - r_t, \quad \tilde{v}_x = \dot{x}\cos\Delta\theta - \dot{y}\sin\Delta\theta$$
$$\tilde{y} = \sqrt{(r_t+x)^2+y^2}\,\Delta\theta, \quad \tilde{v}_y = \dot{x}\sin\Delta\theta + \dot{y}\cos\Delta\theta \tag{A.1}$$

where r_t is the current mean radius of the target's orbit, and $\Delta\theta = \tan^{-1} y/(r_t+x)$. This transformation is illustrated in Fig. 1(b).

rel2dec: relative states are decomposed into a mean and an oscillatory component, $(\tilde{x}_m, \tilde{y}_m)$ and $(\tilde{x}_o, \tilde{y}_o)$, respectively. Schweighart and Sedwick proposed a decomposition that accounts for the secular variations of the J_2 perturbation [18]. Though this transformation is rigorous for circular orbits, small distances and Hill coordinates, it is also valuable for curvilinear variables [35], so that it holds

$$\tilde{x}_m = \frac{4c^2}{2-c^2}\tilde{x} + \frac{2c}{(2-c^2)\omega}\tilde{v}_y, \quad \tilde{x}_o = \tilde{x} - \tilde{x}_m$$
$$\tilde{y}_m = \tilde{y} - \frac{2c}{(2-c^2)\omega}\tilde{v}_x, \quad \tilde{y}_o = \tilde{y} - \tilde{y}_m \tag{A.2}$$

where $c = \sqrt{1+3J_2\,R_e^2/8r_t^2(1+3\cos 2i_t)}$ is the Schweighart Sedwick coefficient, while ω, R_e, and i_t are the orbital pulsation, the Earth radius, and the inclination of the reference orbit of the target, respectively.

Fig. 14 illustrates the chain of transformations that drives to the estimation of the decomposed curvilinear states.

References

[1] T. Williams, Z.S. Wang, Uses of solar radiation pressure for satellite formation flying, Int. J. Robust Nonlinear Control 12 (2002) 163–183.

[2] M.A. Peck, B. Streetman, C.M. Saaj, V. Lappas, Spacecraft formation flying using lorentz forces, J. Br. Interplanet. Soc. 60 (2007) 263–267.

[3] L.B. King, G.G. Parker, S. Deshmukh, J.H. Chong, Spacecraft formation-flying using inter-vehicle coulomb forces, Technical Report, Michigan Technological University, 2002.

[4] C.L. Leonard, Formation keeping of spacecraft via differential drag (M.Sc. thesis), Massachusetts Institute of Technology, Cambridge, 1986.

[5] R. Bevilacqua, M. Romano, Rendezvous maneuvers of multiple spacecraft using differential drag under J_2 perturbation, J. Guid. Control Dyn. 31 (2008) 1595–1607.

[6] R. Bevilacqua, J.S. Hall, M. Romano, Multiple spacecraft assembly maneuvers by differential drag and low thrust engines, Celestial Mech. Dyn. Astron. 106 (2010). 69-8.

[7] D. Pérez, R. Bevilacqua, Differential drag spacecraft rendezvous using an adaptive Lyapunov control strategy, Acta Astronaut. 83 (2013) 196–207.

[8] B.S. Kumar, A. Ng, Bang–Bang Control approach to maneuver spacecraft in a formation with differential drag, in: AIAA Guidance, Navigation and Control Conference, AIAA, Honolulu, 2008.

[9] C. Lambert, B.S. Kumar, J.F. Hamel, A. Ng, Implementation and performance of formation flying using differential drag, Acta Astronaut. 71 (2012) 68–82.

[10] Ben.-O. Yaacov, P. Gurfil, Long-term cluster flight of multiple satellites using differential drag, J. Guid. Control Dyn. 36 (6) (2013) 1731–1740.

[11] A.W. Lewin, Low-cost operation of the ORBCOMM constellation, J. Reduc. Space Mission Cost (1998) 105–117.

[12] G. Bailet, I. Sakraker, T. Scholz, J. Muylaert, Qubesat for aerothermodynamic research and measurement on AblatioN, in: 4th International ARA Days, Arcachon, France, 2013.

[13] A. Ng, C. Lambert, K. Hirako, H. Horiguchi, Y. Nakamura, Japan Canada joint collaboration satellites—design of intersatellite separation mechanism, in: International Astronautical Congress, Prague, 2010.

[14] P. Gurfil, J. Herscovitz, M. Pariente, The SAMSON project-cluster flight and geolocation with three autonomous nano-satellites, in: Small Satellite Conference, Logan, US, 2012.

[15] L. Dell'Elce, G. Kerschen, Comparison between analytical and optimal control techniques in the differential drag based rendez-vous, in: 5th International Conference on Spacecraft Formation Flying Missions and Technologies, Munich, Germany.

[16] B.S. Kumar, A. Ng, Time-optimal low-thrust formation maneuvering using a hybrid linear/nonlinear controller, J. Guid. Control Dyn. 32 (2009) 343–347.

[17] Ben.-O. Yaacov, P. Gurfil, Orbital elements feedback for cluster keeping using differential drag, in: 2nd IAA Conference on Dynamics and Control of Space Systems, Rome, Italy.

[18] S.A. Schweighart, R.J. Sedwick, High-fidelity linearized J2 model for satellite formation flight, J. Guid. Control Dyn. 25 (2002) 1073–1080.

[19] D. Garg, M.A. Patterson, W.W. Hager, A.V. Rao, D.A. Benson, G.T. Huntington, A unified framework for the numerical solution of optimal control problems using pseudospectral methods, Automatica 46 (2010) 1843–1851.

[20] L. Dell'Elce, G. Kerschen, Orbital rendez-vous using differential drag in the QB50 constellation, in: AIAA-AAS Astrodynamics Specialists Conference, Minneapolis, 2012.

[21] L. Dell'Elce, M. Arnst, G. Kerschen, Probabilistic assessment of the lifetime of low-Earth-orbit spacecraft: uncertainty characterization, J. Guid. Control Dyn., 2015, http://dx.doi.org/10.2514/1.G000148.

[22] J.R. Wertz, Spacecraft Attitude Determination and Control, Kluwer Academic Publishers, Dordrecht, The Netherlands, 1978.

[23] M.F. Storz, B.R. Bowman, J.I. Branson, S.J. Casali, W.K. Tobiska, High accuracy satellite drag model (HASDM), Adv. Space Res. 36 (2005) 2497–2505.

[24] F.A. Marcos, New satellite drag modeling capabilities, in: 44th AIAA Aerospace Sciences Meeting and Exhibit, Reno, USA, 2006.

[25] L.H. Sentman, Free Molecule Flow Theory and its Application to the Determination of Aerodynamic Forces, Technical Report, LMSC-448514, Lockheed Missiles & Space Company, 1961.

[26] G.E. Cook, Satellite drag coefficients, Planet. Space Sci. 13 (1965) 929–946.

[27] E. Doornbos, Thermospheric Density and Wind Determination from Satellite Dynamics, Springer-Verlag, Dordrecht, Series: Springer Theses, 2012.

[28] J.M. Picone, A.E. Hedin, D.P. Drob, A.C. Aikin, NRLMSISE-00 empirical model of the atmosphere: statistical comparisons and scientific issues, J. Geophys. Res.: Space Phys. 107 (2002).
[29] M. Zijlstra, S. Theil, Model for Short-term Atmospheric Density Variations, Earth Observation with CHAMP, Springer, Berlin, Heidelberg, 2005.
[30] J. Muylaert, et al., QB50: an international network of 50 cubesats for multi-point, in-situ measurements in the lower thermosphere and for re-entry research, in: ESA Atmospheric Science Conference, Barcelona, Spain, 2009.
[31] H. Heidt, J. Puig-Suari, A. Moore, S. Nakasuka, R. Twiggs, CubeSat: a new generation of picosatellite for education and industry low-cost space experimentation, in: Small Satellite Conference, Logan, US, 2000.
[32] J. Muylaert, Call for CubeSat proposals for QB50, Von Karman Institute for Fluid Dynamics, Brussels, 2012.
[33] B. Wie, Space Vehicle Dynamics and Control, Second edition, AIAA Education Series, Reston, US, 2008.
[34] D.W. Gim, K.T. Alfriend, The state transition matrix of relative motion for the perturbed non-circular reference orbit, in: AAS/AIAA Space Flight Mechanics Meeting, Santa Barbara, 2001.
[35] H. Schaub, Incorporating the secular drifts into the orbit element difference description of relative orbits, in: AAS/AIAA Space Flight Mechanics Meeting, Ponce, 2003.